Journal of Materials Chemistry A

ROYAL SOCIETY OF CHEMISTRY

PAPER

View Article Online
View Journal | View Issue

Open Access Article. Published on 19 August 2025. Downloaded on 2/11/2026 12:09:28 PM.
This article is licensed under a Creative Commons Attribution-NonCommercial 3.0 Unported Licence.

Check for updates

Cite this: J. Mater. Chem. A, 2025, 13, 31592

Investigating structural and morphological transformations of strontium chloride for thermochemical energy storage

Jungho Shin,[a] Madeline R. Morrell,[a] Erik Barbosa,[a] Akanksha K. Menon *[a] and Matthew T. McDowell *[ab]

Received 21st March 2025
Accepted 16th August 2025

DOI: 10.1039/d5ta02326b

rsc.li/materials-a

Thermochemical materials (TCMs) offer a sustainable solution for long-duration thermal energy storage due to their near-lossless energy retention by separating the solid and gas phases. Salt hydrates, which undergo de(hydration) reactions with high reaction enthalpies and low operating temperatures (<100 °C), are particularly promising for applications such as space conditioning and domestic hot water in buildings. However, mechanical degradation of TCMs during (dis)charge cycling is not well understood and limits storage performance. Here, we investigate the structural and morphological changes that occur during (de)hydration cycling of $SrCl_2$, a high-capacity TCM with multiple stable hydrates. *In situ* optical microscopy is used to observe morphological changes and fracture processes in $SrCl_2$ pellets undergoing hydration and dehydration reactions. *In situ* X-ray diffraction and calorimetry/thermogravimetric analysis further elucidate the distinct kinetics governing various $SrCl_2 \cdot xH_2O$ phase transformations, revealing asymmetry during hydration/dehydration and rate limiting transformations. This study provides valuable insight into the phase transformations and mechanical degradation mechanisms of salt hydrate TCMs in pellet form to guide the optimal (dis)charge cycling conditions for stable energy storage performance.

Introduction

Sustainable and low-cost energy storage systems are crucial for enabling intermittent renewable energy to be incorporated onto the grid. Electrochemical energy storage systems, particularly Li-ion batteries, are widely used, as they can efficiently store electrical energy through electrochemical reactions and convert this energy into usable electricity when needed.[1–3] Electrochemical energy storage is particularly advantageous for applications requiring frequent charge/discharge cycling and rapid power delivery, making it ideal for portable electronics and electric vehicles. However, the tendency of batteries to self-discharge makes them less suitable for long-term energy storage over months. Furthermore, their relatively high cost[4,5] and potential supply chain constraints[6,7] limit their use in long-duration energy storage applications.[8]

Thermal energy storage (TES) systems offer significant benefits for stationary and long-duration energy storage at low cost, as they can decouple storage capacity from power output.[9–12] Around 90% of global energy consumption is related to the production, transformation, or use of heat, which incentivizes using TES to store and release thermal energy at a range of temperatures.[13–15] Additionally, TES can be incorporated into buildings and industrial processes, enabling the efficient use of renewable energy sources.[16–18] This integration not only improves energy efficiency but can also replace fossil-based heat sources, thereby promoting decarbonization of the industrial and buildings sectors.[16–18]

Thermochemical materials (TCMs) that undergo hydration and dehydration reactions, such as salt hydrates (*e.g.*, $SrCl_2 \cdot 6H_2O$, $MgSO_4 \cdot 7H_2O$, and $CaCl_2 \cdot 6H_2O$), stand out among TES materials due to the high reaction enthalpies associated with the solid–gas reaction.[19–22] TCM-based systems exhibit relatively high energy density compared to other TES methods such as sensible or latent heat storage (*e.g.*, 200–600 kW h m^{-3} for TCMs *vs.* 50–150 kW h m^{-3} for sensible or latent heat storage materials).[19] Additionally, hydration/dehydration reactions of salt hydrates can occur at temperatures below 100 °C, making them compatible with a wide array of energy sources.[23,24] Furthermore, salt hydrates are abundant, low-cost, and environmentally friendly.[19,25–27] The general hydration/dehydration reaction that these materials undergo is as follows:[28]

$$MX \cdot (n + m)H_2O + \Delta H_r \rightleftarrows MX \cdot nH_2O + mH_2O \quad (1)$$

Here, M represents a metal cation, X represents an anion or polyanion, n and m represent moles of H_2O, and ΔH_r is the

[a]Woodruff School of Mechanical Engineering, Georgia Institute of Technology, Atlanta, GA 30332, USA. E-mail: akanksha.menon@me.gatech.edu; mattmcdowell@gatech.edu
[b]School of Materials Science and Engineering, Georgia Institute of Technology, Atlanta, GA 30332, USA

This journal is © The Royal Society of Chemistry 2025

Open Access Article. Published on 19 August 2025. Downloaded on 2/11/2026 12:09:28 PM. This article is licensed under a Creative Commons Attribution-NonCommercial 3.0 Unported Licence.

enthalpy of the reaction. Upon exposure to higher temperatures and lower humidity (vapor pressure) conditions (*e.g.*, during the day), TCMs undergo endothermic dehydration reactions (eqn (1)), releasing water vapor and storing thermal energy, thereby "charging" the system. When exposed to lower temperatures and higher humidity conditions (*e.g.*, during the night), the dehydrated salt undergoes an exothermic hydration reaction with water vapor (eqn (1)), thereby releasing the stored energy as heat and "discharging" the system. These spontaneous reaction processes enable salt hydrates to store renewable energy (*e.g.*, using solar collectors or off-peak grid electricity) when it is available and release that energy when needed (*e.g.*, using cool, humid air), which is ideal for heating and air conditioning in buildings.[29]

Recent research has focused on hydration/dehydration reactions in salt hydrates for TES.[19–22,30,31] Kiyabu *et al.* used DFT calculations to estimate the energy densities, operational temperature ranges, and thermodynamic stabilities of various salt hydrates.[30] They identified several metal fluorides as stable TES materials with exceptional energy densities and operating temperatures ideal for domestic heating and intermediate-temperature applications. Clark *et al.* experimentally assessed the thermochemical cycling behaviour of various salt hydrates ($SrCl_2$, $MgSO_4$, Na_3PO_4, $MgCl_2$, and $SrBr_2$), identifying promising candidates for practical use.[31] Barbosa *et al.* evaluated the hydration behaviour of binary salt mixtures of $MgCl_2$ and $SrCl_2$, highlighting their improved kinetics over a wide range of vapor pressures.[28]

Despite the numerous advantages of salt hydrate-based TCMs, their practical realization remains challenging due to their relatively poor long-term cyclability.[19,21,32] These materials undergo significant volume and structural changes during hydration/dehydration cycling, leading to mechanical instabilities and degradation of energy storage capacity.[19,21] For instance, it has been found that K_2CO_3 pellets undergo morphological changes during hydration/dehydration cycling, leading to the formation of isolated pores and a highly tortuous pore system.[21] These morphological changes can inhibit mass (water vapor) transport, resulting in reduced power output. Martin *et al.* identified a critical particle size ~10 μm, below which mechanical instabilities were minimized in ball-milled $SrCl_2$ powders during hydration/dehydration cycling.[19] Researchers have also explored the development of composite structures, where the host matrices (*e.g.*, expanded graphite or alginate) are inert and provide mechanical stability to the salt, thus enhancing cycling performance.[33–36] However, composites present other challenges such as the added mass of inert material, which reduces specific energy storage capacity.[19] To successfully implement TES systems using salt hydrates, it is crucial to better understand their phase transformation and degradation mechanisms to effectively control and optimize their cyclic transformation behaviour. In particular, there is a need to directly investigate their dynamic evolution in real time to understand how material transformations and morphological/structural changes are linked in form factors that are relevant for the application (*i.e.*, as pellets instead of powders that are typically reported in literature).[19,28]

Here, we investigate the structural and morphological evolution of the strontium chloride ($SrCl_2$) TCM during hydration/dehydration cycling using correlated *in situ* characterization techniques. *In situ* optical microscopy under controlled temperature and humidity conditions was used to observe dynamic morphological changes of $SrCl_2$ pellets. *In situ* X-ray diffraction (XRD) analysis revealed the kinetics of phase transformations during material hydration and dehydration, which was further correlated to calorimetry and thermogravimetric analysis. These results provide insight into mechanical fracture processes that occur during thermochemical transformations, as well as distinct reaction kinetics associated with the evolution of different phases; these aspects are important to control for optimized reaction reversibility and stable storage performance.

Results and discussion

In this study, $SrCl_2$ was selected amongst various candidate TCMs due to its stability at ambient conditions and relatively low hydration/dehydration temperatures (<100 °C). Additionally, deliquescence of $SrCl_2$ occurs only under high relative humidity (>~70% relative humidity, RH) at room temperature (25 °C). This material has been studied in powder form,[19,28] but the lack of studies on the pellet form hinder its use in packed bed TES reactor applications. Dehydration (charging) of $SrCl_2$ under high-temperature, low-humidity conditions and hydration (discharging) under low-temperature, high humidity conditions cause substantial volumetric and morphological changes in the salt hydrate pellet, as shown in in Fig. 1. According to the phase diagram (Fig. S1), $SrCl_2$ exhibits four thermodynamically stable hydrated phases depending on temperature and humidity: anhydrous $SrCl_2$, $SrCl_2$ monohydrate ($SrCl_2 \cdot H_2O$), $SrCl_2$ dihydrate ($SrCl_2 \cdot 2H_2O$), and $SrCl_2$ hexahydrate ($SrCl_2 \cdot 6H_2O$). This adds complexity compared to simple salt hydrates such as K_2CO_3 and $SrBr_2$ that exhibit a single hydration/dehydration transition. From this phase diagram, we selected the hydration conditions in these experiments to be 25 °C (room temperature) and 60% RH to form the hexahydrate, while dehydration conditions were 80 °C and 0.1% RH to form the anhydrous salt. This allows for hydration of $SrCl_2$ without deliquescence, which can lead to salt agglomeration.[37]

To monitor the morphological evolution of $SrCl_2$ during dehydration and hydration, *in situ* optical microscopy was carried out under controlled humidity and temperature conditions (see Methods and Fig. S2). To facilitate the observation of sample cracking, the sample was preconditioned at 25 °C and 60% RH and subsequently pelletized in the hydrated form. Fig. 2 and S3 show the morphological changes of a $SrCl_2$ pellet during dehydration and hydration. The $SrCl_2$ pellet, which initially had few cracks in its hexahydrate state (Fig. 2a), showed surface fracture during dehydration, which was caused by the volume contraction when H_2O leaves the material. Upon further dehydration, more cracks appeared, and the existing cracks were extended and widened as additional H_2O leaves the material (Fig. 2b–d). These observations are further supported

Open Access Article. Published on 19 August 2025. Downloaded on 2/11/2026 12:09:28 PM.
This article is licensed under a Creative Commons Attribution-NonCommercial 3.0 Unported Licence.

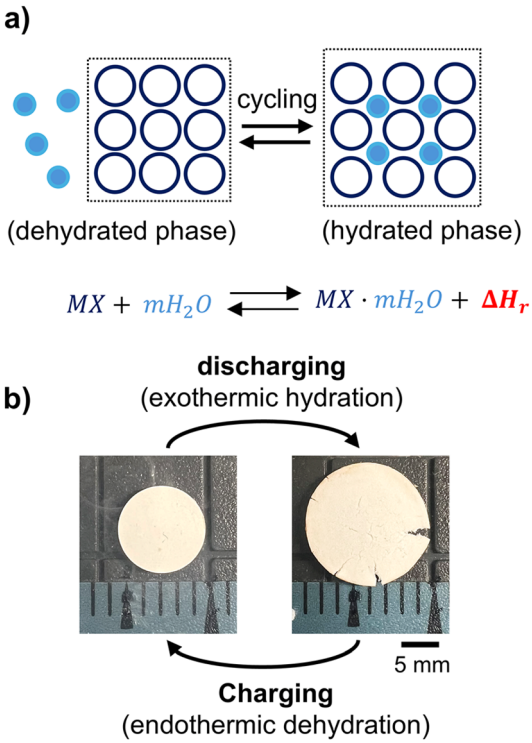

Fig. 1 (a) Schematic illustrating hydration and dehydration of a TCM resulting in crystal structure evolution. (b) Photographs showing the volume change of a $SrCl_2$ pellet during hydration (discharging) and dehydration (charging). The theoretical volumetric expansion of the strontium chloride from the fully dehydrated to the hydrated state is 165%, as discussed subsequently.

by high-magnification SEM images (Fig. S4), which reveal the formation of microscale cracks in the dehydrated $SrCl_2$ pellet. During hydration (Fig. 2e–h), volume expansion caused the previously formed cracks to close. This suggests a reversible process in that the pellet returns to its initial state after one dehydration/hydration cycle. With continued cycling, however, more severe mechanical damage occurred after each cycle; morphological changes after increasing numbers of cycles are presented in the dehydrated state in Fig. 3a–f.[21]

From these imaging experiments, we identified two primary mechanisms of crack formation in $SrCl_2$ due to hydration/dehydration (Fig. 3g and h). First, the mechanical stresses induced by uneven volume contraction within the pellet result in cracks that grow parallel to the H_2O transport path. The $SrCl_2$ pellet likely exhibits a nonuniform distribution of H_2O concentration (and thus dehydrated phases) along the path due to limited rates of H_2O diffusion. This gradient in the extent of dehydration would lead to nonuniform volume contraction along the diffusion path, which would cause biaxial tensile stresses to be generated in the near-surface regions under the constraint of the rest of the pellet. This behaviour causes cracks to form parallel to the diffusion path (Fig. 3g). These cracks initially emerge at the microscale and progressively enlarge through coalescence as dehydration advances, eventually evolving into prominent fractures (Fig. S4). Second, nonuniform volume changes of grains within the pellet may result in interfacial sliding and the initiation and propagation of cracks with varying directionalities, ultimately compromising the structural integrity of the pellet (Fig. 3h). Repeated cycling worsens both types of cracks, eventually leading to pulverization of the material. Such pulverization induced by hygrothermal cycling can create more tortuous transport paths for moisture and heat, thereby altering the kinetics of subsequent cycles and reducing thermal storage capacity.[38–40] Furthermore, the increased surface area and porosity due to cracking could result in more rapid and less uniform heat absorption and release as cycling progresses, thereby reducing thermal storage capacity and power output.

While *in situ* optical microscopy captures macro- and microscale morphological changes due to cracking and mechanical degradation, these observations highlight the need

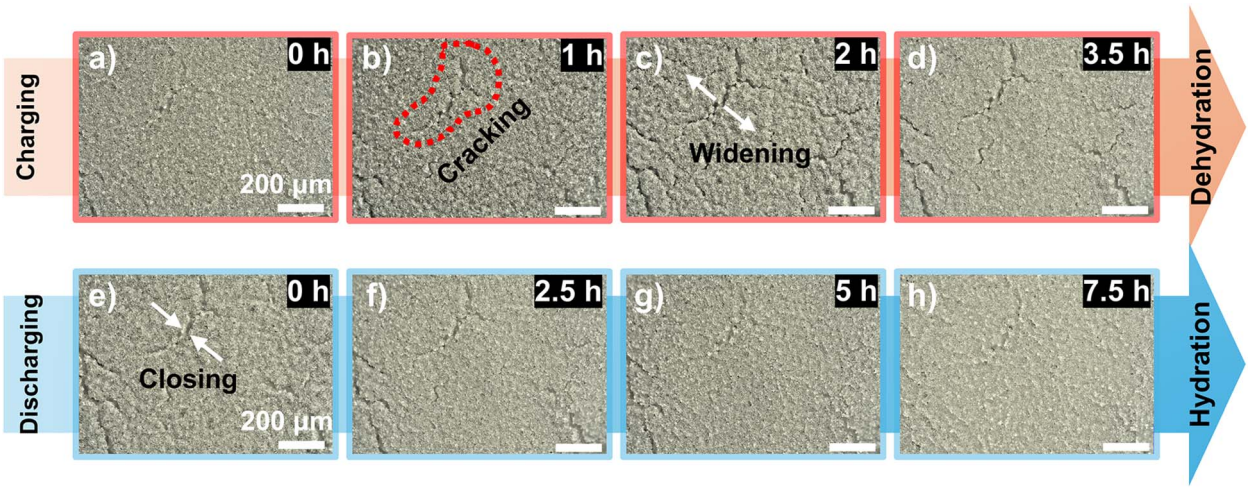

Fig. 2 *In situ* optical microscopy of the morphological evolution of the top surface of a $SrCl_2$ pellet during (a–d) charging (dehydration) and (e–h) discharging (hydration). Images were captured every minute during charging and discharging. Lower-magnification images can be found in Fig. S3.

 This journal is © The Royal Society of Chemistry 2025

Open Access Article. Published on 19 August 2025. Downloaded on 2/11/2026 12:09:28 PM.
This article is licensed under a Creative Commons Attribution-NonCommercial 3.0 Unported Licence.

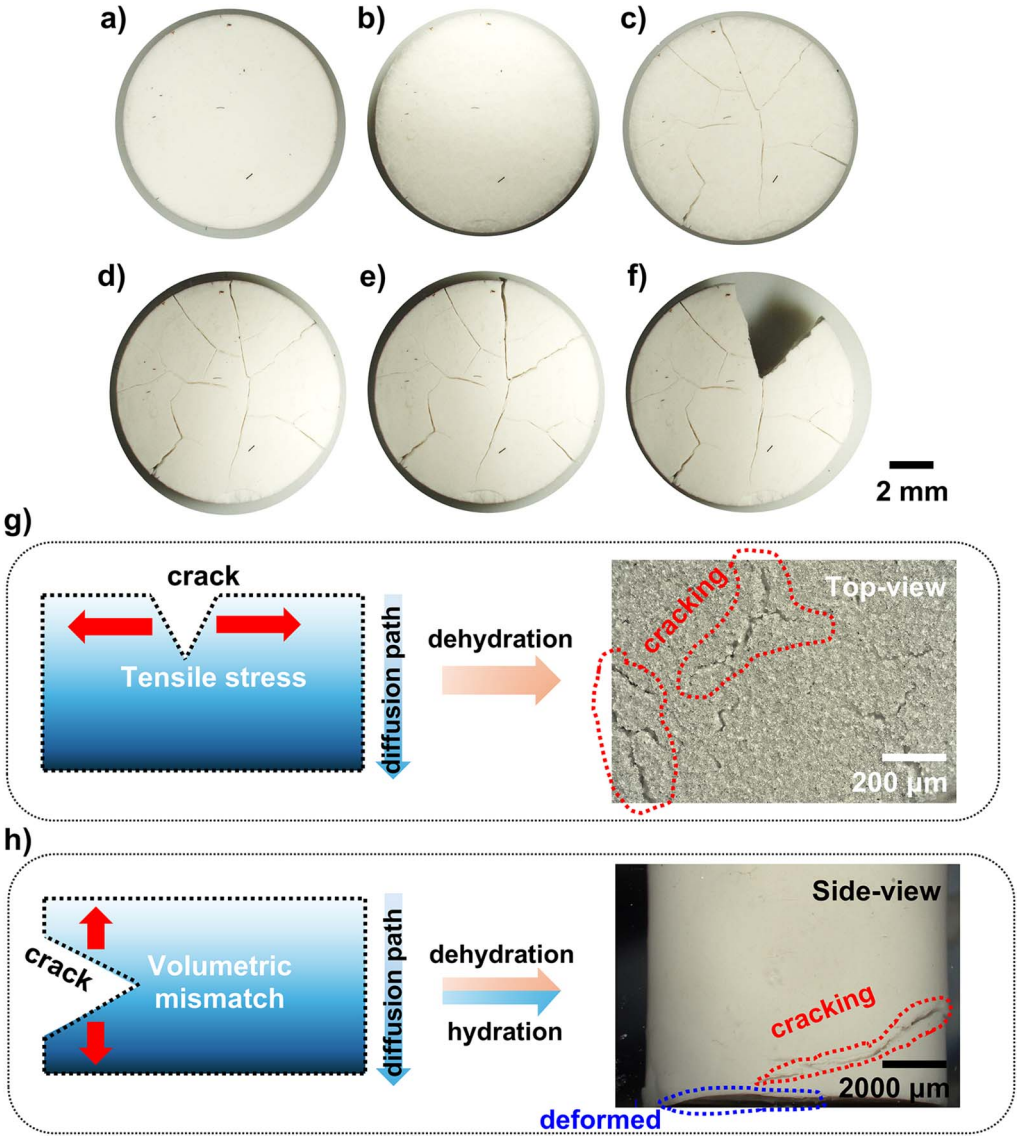

Fig. 3 Optical microscopy images of the top surface of a $SrCl_2$ pellet in the dehydrated state after undergoing multiple hydration/dehydration cycles: (a) as prepared, (b) after one cycle, (c) after two cycles, (d) after three cycles, (e) after four cycles, and (f) after five cycles. (g and h) Schematics of crack formation mechanisms induced by hydration/dehydration cycling, highlighting (g) biaxial stress generation resulting in cracks along the H_2O diffusion path and (h) nonuniform volume changes of various regions resulting in cracks with different directionality. In (g) and (h), the left schematics depict the mechanisms, while the right ones show microscopy images capturing the corresponding phenomena.

to examine the underlying crystal structure transformations related to this behaviour. As such, *in situ* XRD measurements were carried out to track phase transformation processes (Fig. 4). Prior to *in situ* XRD measurements of the dehydration process, the $SrCl_2$ pellet was stored in a chamber at 25 °C and 60% RH for 24 h to ensure its hydrated state, resulting in the formation of a mixture of $SrCl_2 \cdot 6H_2O$ and $SrCl_2 \cdot 2H_2O$ (Fig. 4a). Although the phase diagram suggests that the hexahydrate is the stable phase under these conditions, the presence of dihydrate suggests kinetic limitations to full hydration (*i.e.*, slow diffusion of water vapor or limited reaction kinetics). With this hydrated starting material, *in situ* XRD measurements during dehydration were performed at 80 °C and 0.1% RH (Fig. S5a) for 7 h. The dehydration transformation processes (Fig. 4b–d) show that there is first a transformation from the $SrCl_2 \cdot 6H_2O$–$SrCl_2 \cdot 2H_2O$ mixture to fully form $SrCl_2 \cdot 2H_2O$, followed by the transformation to $SrCl_2 \cdot H_2O$, and finally to anhydrous $SrCl_2$. Additionally, multiple phases were observed simultaneously during *in situ* XRD, indicating a gradual and stepwise phase transformation process. This dehydration process through multiple intermediate phases is in contrast to other salts (such as K_2CO_3 or $SrBr_2$) that undergo a single-step phase transformation without intermediate phases during thermochemical cycling.[41–43] Notably, all the phases measured for $SrCl_2$ are crystalline with distinct diffraction patterns (Fig. 4b). In Fig. 4c, which is a magnified view of Fig. 4b over the first 0.5 h, the $SrCl_2 \cdot 6H_2O$ underwent relatively fast dehydration to $SrCl_2 \cdot 2H_2O$ within the first 10 min. Subsequently, $SrCl_2 \cdot 2H_2O$ was

Open Access Article. Published on 19 August 2025. Downloaded on 2/11/2026 12:09:28 PM.
This article is licensed under a Creative Commons Attribution-NonCommercial 3.0 Unported Licence.

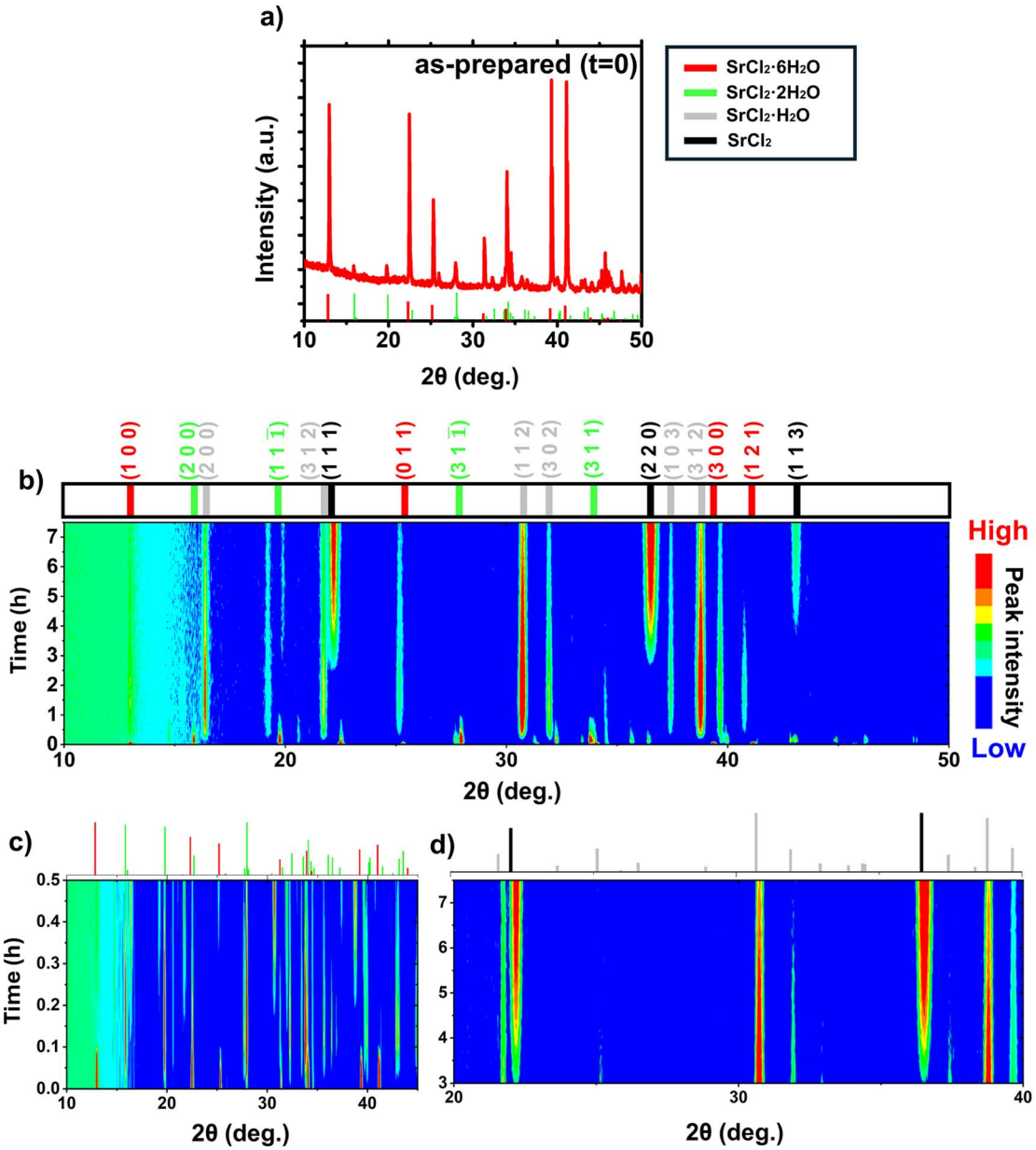

Fig. 4 *In situ* XRD measurements during dehydration. (a) XRD patterns of the as-prepared hydrated $SrCl_2$ pellet, which is a mixture of $SrCl_2 \cdot 6H_2O$ and $SrCl_2 \cdot 2H_2O$. (b) Evolution of XRD patterns during dehydration at 80 °C and 0.1% RH, with detailed conditions provided in Fig. S4. (c and d) Magnified views of the XRD patterns for the time intervals of (c) 0–0.5 h and (d) 3–7.5 h. Reference patterns for $SrCl_2$ (cubic, JCPDS: 00-006-0537), $SrCl_2 \cdot H_2O$ (orthorhombic, JCPDS: 04-010-2950), $SrCl_2 \cdot 2H_2O$ (monoclinic, JCPDS: 00-025-0891), and $SrCl_2 \cdot 6H_2O$ (trigonal, JCPDS: 04-010-2982) are shown above each spectrum for comparison, with coloured peak indicators corresponding to the phases in the legend in (a).

dehydrated to $SrCl_2 \cdot H_2O$ during the first hour, after which $SrCl_2 \cdot H_2O$ remained as the dominant phase for an extended period of 2 h. Afterwards, the final phase transformation from $SrCl_2 \cdot H_2O$ to the anhydrous phase occurred gradually over approximately 3 h, and dehydration was not fully complete by the end of the experiment (Fig. 4d). As a result, monohydrate peaks were still observed; we expect complete dehydration to the anhydrous state to take place under these conditions over longer durations beyond this experiment, again suggesting kinetic limitations (*i.e.*, nucleation barriers that result in a metastable zone around the equilibrium phase boundary).[37] The relatively rapid phase transformation from $SrCl_2 \cdot 6H_2O$ to $SrCl_2 \cdot H_2O$ in the early stages, followed by the slower transformation from $SrCl_2 \cdot H_2O$ to the anhydrous $SrCl_2$ phase, aligns with simultaneous thermal analysis data showing mass change and heat flow over time (Fig. 5), which is discussed subsequently.

In situ XRD during hydration was conducted on a separate sample under conditions of 25 °C and 40% RH (Fig. S5), with results shown in Fig. S6. 40% RH was selected due to equipment limitations (see the Methods section); based on the phase diagram in Fig. S1, $SrCl_2 \cdot 6H_2O$ is the equilibrium phase at 25 °C

 This journal is © The Royal Society of Chemistry 2025

Open Access Article. Published on 19 August 2025. Downloaded on 2/11/2026 12:09:28 PM.
This article is licensed under a Creative Commons Attribution-NonCommercial 3.0 Unported Licence.

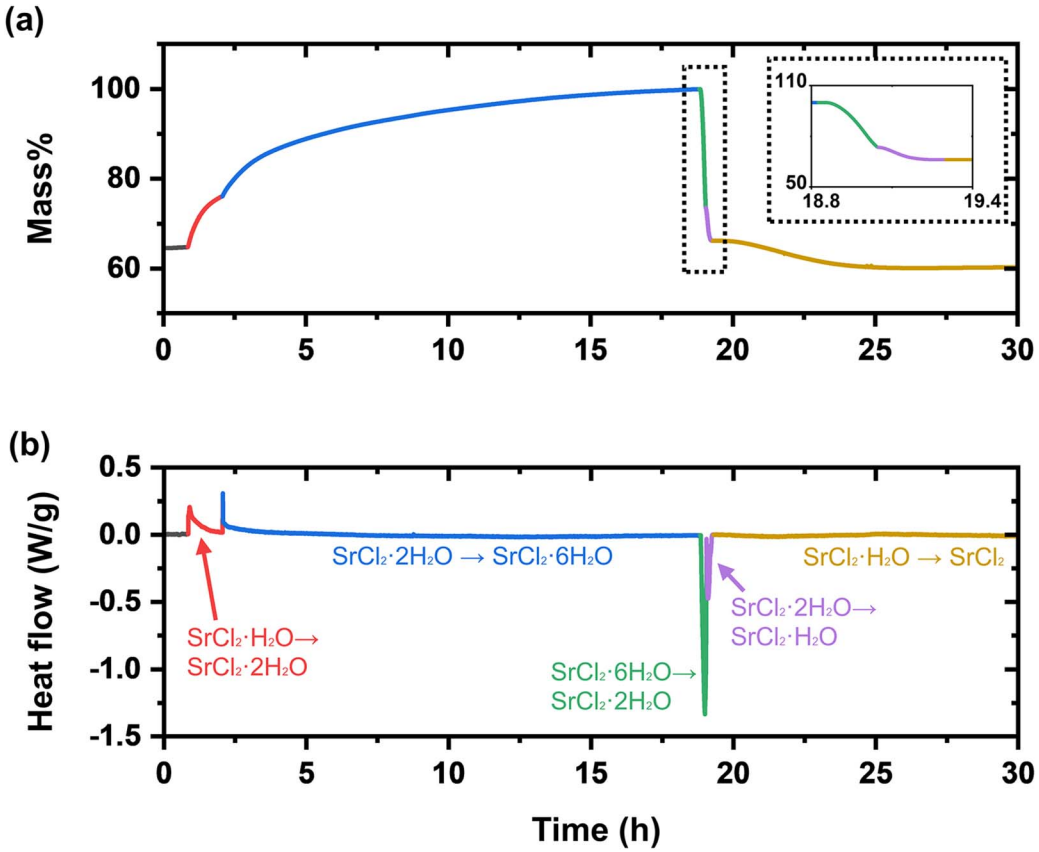

Fig. 5 Plots showing the measured (a) relative mass and (b) heat flow of a $SrCl_2$ pellet during hydration and dehydration at constant temperature and RH values. Hydration was carried out at 25 °C and 60% RH, and dehydration at 80 °C and 0.1% RH. The pellet had an initial relative density of 91% and an initial sample mass of 10 mg. The mass is relative to the maximum sample mass (*i.e.*, the mass of $SrCl_2 \cdot 6H_2O$ is 100%); Table S1 shows the theoretical mass percent values associated with each of the stable hydrates of $SrCl_2$. Anhydrous $SrCl_2$ is 59.4% of the hexahydrate mass. Each phase transformation region is highlighted with different colours, and they are labeled in (b). In (a), the inset is a magnified view to better visualize the dehydration phase transformations.

and 40% RH. Initially, the sample was a mixture of the anhydrous and monohydrate phases. It rapidly hydrated within the first 0.5 h (Fig. S6c), during which it transitioned to $SrCl_2 \cdot 2H_2O$ relatively quickly. The dihydrate phase remained present for an extended period (>8 h) before eventually forming $SrCl_2 \cdot 6H_2O$ (Fig. S6d). At the end of the ~17 h experiment, a mixture of the hexahydrate and dihydrate phases was present, suggesting that complete hydration to the hexahydrate state occurs over longer durations than this experiment.

Fig. S7 presents magnified views of the *in situ* XRD of the monohydrate phase during dehydration and the dihydrate phase during hydration, which are the most persistent phases observed during the measurements. No obvious XRD peak shifts were observed during dehydration, indicating a lack of substantial stresses/strains within the crystal structures. During hydration, there is a minor $2\theta = 0.03°$ shift of the peak to higher 2θ values. The lack of more substantial peak shifts suggests that the observed fracture, microcracks, and/or internal porosity formation dissipate strain energy effectively, rather than inducing substantial elastic strain in the lattice.

Fig. 5 presents mass change and heat flow measurements of a pressed $SrCl_2$ pellet as a function of time for one hydration and dehydration step. The $SrCl_2$ pellet was preconditioned for 12 hours at 50 °C and 12% RH (Fig. S1) to obtain the monohydrate phase prior to running the simultaneous thermal analysis (thermogravimetric analysis/differential scanning calorimetry, TGA/DSC). The phase transformation kinetics are observable in the gravimetric data (Fig. 5a), being characterized by an initial fast mass increase followed by a gradual plateau. During hydration, a transition from $SrCl_2 \cdot H_2O$ to $SrCl_2 \cdot 2H_2O$ occurs over ~1.2 hours, and the subsequent transition from $SrCl_2 \cdot 2H_2O$ to $SrCl_2 \cdot 6H_2O$ takes place over a significantly longer period (~15.9 hours). During dehydration, three phase transformations are observed: a rapid initial mass reduction from $SrCl_2 \cdot 6H_2O$ to $SrCl_2 \cdot 2H_2O$ over ~0.2 h and $SrCl_2 \cdot 2H_2O$ to $SrCl_2 \cdot H_2O$ over ~0.2 h, followed by a slower mass decrease from $SrCl_2 \cdot H_2O$ to anhydrous $SrCl_2$ over ~10.8 h. These transitions are consistent with the gray dotted arrow in the phase diagram in Fig. S1, corresponding to traversing of the phase boundaries during hydration and dehydration. The experimentally measured mass changes in Fig. 5b agree with the theoretical values shown in Table S1.

Each phase transformation corresponds to a distinct heat flow peak (a positive peak is exothermic, while a negative peak is

Open Access Article. Published on 19 August 2025. Downloaded on 2/11/2026 12:09:28 PM.
This article is licensed under a Creative Commons Attribution-NonCommercial 3.0 Unported Licence.

endothermic), as shown in Fig. 5b. During hydration, separate exothermic peaks for both the monohydrate to dihydrate and dihydrate to hexahydrate transitions are observed, with respective gravimetric energy density (GED) values of 260.7 J g^{-1} and 584.5 J g^{-1}. During dehydration, two endothermic peaks correspond to sequential transformations from $SrCl_2 \cdot 6H_2O$ to $SrCl_2 \cdot 2H_2O$ to $SrCl_2 \cdot H_2O$ are present at the initial stages of the experiment; these GED values correspond to 600.3 J g^{-1} and 296.6 J g^{-1}. These transitions are followed by sluggish transformation from $SrCl_2 \cdot H_2O$ to anhydrous $SrCl_2$ over a prolonged period. The peak corresponding to this final transition cannot be distinctly resolved due to its small magnitude; however, it is clearly identifiable in the mass decrease in Fig. 5a (detailed analysis of the energy density and enthalpy for each phase transition can be found in SI Note S1 and Table S3).

By correlating the simultaneous thermal analysis (TGA/DSC) results to the *in situ* XRD measurements, we observe an asymmetry in the hydration and dehydration behaviour of $SrCl_2$. In other words, the material remains in different intermediate hydration states for extended periods during hydration *vs.* dehydration. During hydration, the dihydrate forms rapidly and persists, as evidenced by the gradual increase in slope of the TGA curve and the flatter region between 2.1 and 18 h. This behaviour corresponds to the phase transformation from the dihydrate to the hexahydrate, as confirmed by *in situ* XRD. The slow kinetics of this phase transformation from dihydrate to hexahydrate can be attributed to combination of substantial structural rearrangement (Fig. S8 and Table S2), a nucleation barrier within the metastable dihydrate matrix, and a relatively low thermodynamic driving force under our hydration conditions (25 °C and 40% RH for *in situ* XRD and 25 °C and 60% RH for TGA/DSC).[37] This behaviour is further supported by the gradual weight increase in Fig. 5a, highlighting the sluggish kinetics of the $SrCl_2 \cdot 2H_2O$ to $SrCl_2 \cdot 6H_2O$ phase transformation. Considering the faster transformation from anhydrous $SrCl_2$ through $SrCl_2 \cdot H_2O$ to $SrCl_2 \cdot 2H_2O$, each phase transformation exhibits markedly different kinetics under the given temperature and humidity conditions. Modifying conditions to improve the hydration kinetics (*e.g.*, through increasing humidity) may push the system into deliquescence (Fig. S1), which eliminates the porous microstructure and can degrade transport pathways.

In contrast, during dehydration, both XRD and TGA/DSC showed that $SrCl_2 \cdot H_2O$ did not quickly transition to the anhydrous state even under relatively high temperature and low

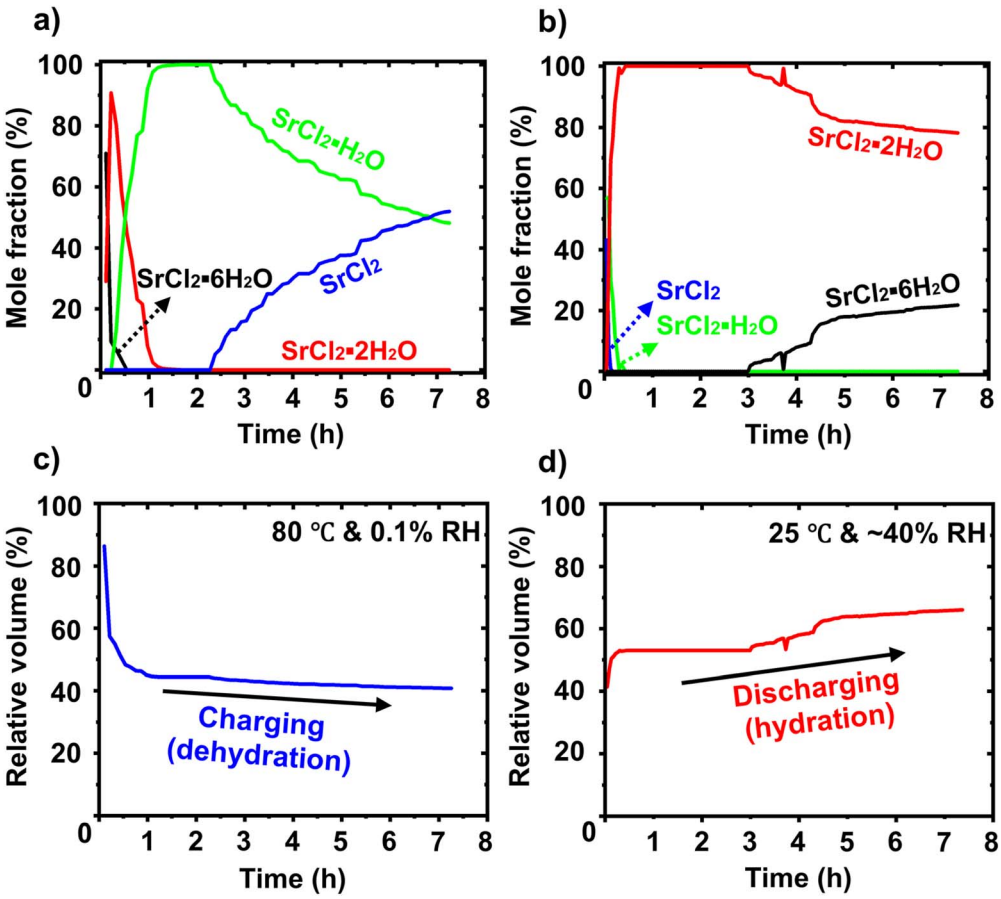

Fig. 6 (a and b) Quantitative analysis of the mole fraction of each phase during (a) dehydration and (b) hydration using whole pattern fitting of the XRD data in Fig. 4 and S6. (c and d) Estimate of the volume changes of the $SrCl_2$ pellet over time during (c) charging (dehydration) and (d) discharging (hydration). For (c) and (d), the volumes were calculated based on the gravimetric ratios and lattice parameters (Table S2) and normalized based on 100% volume being $SrCl_2 \cdot 6H_2O$.

 This journal is © The Royal Society of Chemistry 2025

Open Access Article. Published on 19 August 2025. Downloaded on 2/11/2026 12:09:28 PM.
This article is licensed under a Creative Commons Attribution-NonCommercial 3.0 Unported Licence.

humidity conditions (80 °C and 0.1% RH). This sluggish transformation is likely due to the broad metastable zone of the monohydrate and the limited thermodynamic driving force near the equilibrium boundary.[37] To further support, the heat flow peak associated with this transformation was barely discernible, likely due to a combination of relatively high enthalpy ($\Delta_r H$) (Table S3), sluggish transport kinetics, and possible limitations (*e.g.*, constraints in phase boundary movement) of our experimental conditions. Similar to what we observed with hydration, during dehydration these phase transformations exhibit different kinetics under the given temperature and humidity conditions, resulting in phase-dependent and directionally asymmetric reaction rates during thermal cycling.

It should be noted that the discrepancy in timescales between TGA/DSC and XRD can be attributed to the different sample sizes for the different measurements, as well as the inherently limited penetration depth of X-rays, which predominantly analyses only the near-surface region of the sample. Nevertheless, the relative time duration of each phase transformation (compared to the total phase transformation time) aligns closely between the two measurements.

To quantitatively determine the fraction of each phase as a function of time, we performed whole pattern fitting of the XRD data, as shown in Fig. 6. This method analyses the predefined patterns of different phases (*e.g.*, anhydrous, monohydrate, dihydrate, and hexahydrate) and compares it with the measured XRD pattern to estimate the quantity of each phase. Fig. 6a and b show the variation of the mole fractions of each phase during dehydration and hydration. This analysis quantifies the extended retention of $SrCl_2 \cdot H_2O$ during dehydration (Fig. 6a) and the dihydrate during hydration (Fig. 6b). Under our experimental conditions for XRD (80 °C and 0.1% RH for dehydration and 25 °C and ~40% RH for hydration), it is clear that dehydration proceeded more rapidly than hydration in the near-surface region of the sample probed by XRD, and the final stages of each process appear to be sluggish.

Using the lattice parameters of the crystal structures of the various phases (Table S2), we calculated both the unit cell volume ($Å^3$) and the unit cell volume per Sr atom ($Å^3$/Sr), as shown in Fig. S9. The unit cell volume divided by the number of Sr atoms per unit cell provides a measure of the relative volume change due to the hydration/dehydration transformations. Based on these calculations, the theoretical volume expansion associated with full hydration (*i.e.*, going from $SrCl_2$ to $SrCl_2 \cdot 6H_2O$) is approximately 165%. From the *in situ* imaging in Fig. 2 and S3, we measured a volume change of 119%. The discrepancy between the measured and theoretical values may be due to several factors, including (i) the initial sample pellet exhibiting less than 100% relative density with porosity that can accommodate expansion, (ii) the initial sample not being fully dehydrated, (iii) partial hydration occurring during sample transfer, and (iv) limitations of top-view optical microscopy, which may not capture out-of-plane deformation such as pellet bending during cycling. Nevertheless, the general agreement between our measurements and theory highlights the substantial volume changes associated with these hygrothermal transformations.

By combining the mole fraction changes over time from XRD (Fig. 6a and b) and the normalized volume of each phase (Fig. S9b), we calculated the volume changes as a function of time during dehydration and hydration, with the relative volume with time shown in Fig. 6c and d. The relative volume is normalized based on the fully hydrated $SrCl_2 \cdot 6H_2O$ being classified as 100%. The relative volumes of the hydrated phases are as follows: 37.6% for $SrCl_2$, 44.4% for $SrCl_2 \cdot H_2O$, 53.1% for $SrCl_2 \cdot 2H_2O$, and 100% for $SrCl_2 \cdot 6H_2O$. During dehydration, the relative volume decreases from 86.4% (the material is a mixture of the hexahydrate and dihydrate phases) rapidly during the first hour followed by a more gradual decline. During hydration, the relative volume increases from 41.4% (the material is a mixture of the anhydrous and monohydrate phases) sharply over the first 40 min, after which the increase is much more gradual. Thus, in both the dehydration and hydration processes, initial rapid volume changes were observed, followed by relatively slow volume changes due to slowed reaction processes (kinetics). We emphasize that these findings are derived from the XRD data, which capture the near-surface regions, and that the overall pellet likely continues to change volume. Recalling Fig. 3g and h, nonuniform hydration levels along the diffusion path can generate mechanical stresses and cause mismatched volume changes, which can cause crack formation. By applying those scenarios into the volume changes over time, these rapid and abrupt crystal structure changes in the early stages of hydration and dehydration can likely generate more substantial mechanical stresses and volumetric mismatch within the material, leading to micro- to macro-scale cracking and mechanical degradation.

Finally, we investigated the crystal structure over multiple dehydration/hydration cycles. Fig. 7 shows *ex situ* XRD patterns of a sample after undergoing 1, 3, 5, and 10 cycles. The crystallinity of the $SrCl_2 \cdot 6H_2O$ was retained without obvious change in peak intensities, indicating the absence of amorphization or other phenomena such as grain refinement. This suggests relatively reversible crystal structure evolution over multiple cycles.

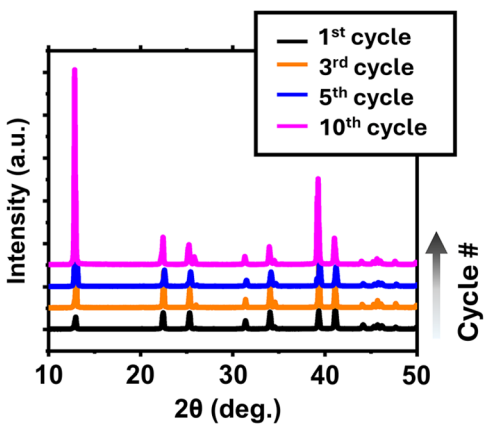

Fig. 7 XRD patterns of $SrCl_2 \cdot 6H_2O$ after one (black), three (orange), five (blue), ten (pink) cycles.

Open Access Article. Published on 19 August 2025. Downloaded on 2/11/2026 12:09:28 PM. This article is licensed under a Creative Commons Attribution-NonCommercial 3.0 Unported Licence.

However, while the transformations of the crystal structure are sustained over multiple cycles, mechanical degradation at larger length scales, such as micro- and macro-scale cracking, still occur, potentially resulting in irregular energy output rates in TES systems. Further work is needed to understand chemo-mechanical evolution across hundreds or thousands of cycles, and strategies such as the use of binder additives or host matrix materials could be useful for mitigating mechanical damage.

Conclusion

We have investigated the phase transformations, volume changes, and chemo-mechanical degradation processes of $SrCl_2$ as a thermochemical energy storage material that features multiple hydration states. $SrCl_2$ pellets prepared without any supporting porous matrix or binder were used to isolate degradation driven purely by chemo-mechanical effects of the material. *In situ* optical microscopy revealed that dehydration/hydration processes induce substantial mechanical deformation in the material during the uptake and release of water vapor, which ultimately results in the formation of cracks. Based on our observations, we propose crack formation mechanisms determined by the mismatch in volume changes along the H_2O transport path, as well as to nonuniform hydration of granular material. *In situ* XRD was conducted during hygrothermal cycling to evaluate the structural evolution of $SrCl_2$, resulting in measurement of the kinetics of the various reactions, as well as the rate of volume change of the material. The experimentally observed volume change is comparable to that calculated from crystal structure analysis (119% *vs.* 165%). By combining *in situ* XRD and simultaneous thermal analysis measurements (TGA/DSC), we revealed that hydration and dehydration of different phases feature distinct kinetics. Furthermore, rapid volume changes were found to occur in the early stages of hydration and dehydration, which can exacerbate fracture. Such mechanical degradation can alter H_2O and heat transport, resulting in unstable thermal energy storage performance and material pulverization with cycling.

Overall, this study provides fundamental insights into the thermo-chemo-mechanical behaviour of $SrCl_2$ salt during hygrothermal cycling, which is important information for its use in future TES systems. These findings may guide the optimization of operating conditions in such systems. The asymmetric hydration and dehydration transformation behaviours of $SrCl_2$ are important to design and control for in the development of effective TES systems. The different transformation rates of the various phases suggest that heat absorption and release rates can vary over time, which may present challenges for achieving stable and controlled thermal power output during operation. By identifying the sluggish transitions, which in turn impact cyclability, the optimal "state of charge" can be defined for a given thermochemical material. For instance, instead of cycling from 0% to 100% state of charge, one might consider operating within a narrower range (such as between the monohydrate and dihydrate phases) to avoid inefficient energy storage and/or mechanical degradation. This action would have the trade-off of reduced energy storage capacity.

Finally, while $SrCl_2$ exhibits complex phase transformation and volume change behaviour due to multiple intermediate phases, simple salt hydrates with single-step transitions, such as K_2CO_3 or $SrBr_2$, are expected to undergo more uniform stress evolution, potentially altering the mechanical degradation behaviour. It would be of interest in future studies to systematically compare the chemo-mechanical degradation behaviours of single- and multi-phase salt hydrates to elucidate the role of phase complexity in stress evolution and fracture. Furthermore, understanding how external constraints (such as pellet fabrication pressure and casing-induced confinement), composite architectures, and engineered porosity contribute to stress accommodation and mechanical stability will be critical for the development of more durable thermochemical energy storage materials.

Methods

Sample preparation

$SrCl_2$ (VWR, anhydrous, purity of >99.5%) was stored in an N_2-filled glovebox to prevent moisture exposure. The particle size of as-received $SrCl_2$ powder was measured to be 9.9 μm ± 5.8 μm (average ± standard deviation) using the linear intercept technique (Fig. S10).

$SrCl_2$ pellets were prepared with various initial hydration states for different experiments. For *in situ* optical microscopy, where dehydration-induced crack formation was the focus, $SrCl_2$ powder was preconditioned at 25 °C and 60% RH overnight to ensure its fully hydrated phase ($SrCl_2 \cdot 6H_2O$). It was then pressed into pellets under ambient conditions. In contrast, for *in situ* XRD hydration experiments, pellets were made from dehydrated $SrCl_2$. The powder was preconditioned under vacuum at 80 °C overnight and pelletized under an inert atmosphere. For *in situ* XRD dehydration measurements, pellets were again prepared from the fully hydrated phase following the same protocol as for optical microscopy. 10 mm diameter pellets were prepared by uniaxially pressing at 3 tons, achieving a relatively high relative density of ~91% in the dehydrated state. The pellets were then sealed and transferred to the testing set-up to avoid any undesirable reaction in air during transport. The relative density of a $SrCl_2$ pellet was estimated by comparing its measured density (mass/volume) to the theoretical crystal density of $SrCl_2$ (3.052 g cm^{-3}). The volume was calculated based on its radius (r) and thickness (h), assuming the pellet to be a perfect cylinder (*i.e.*, volume = $r^2\pi h$), and the mass was measured using a Radwag AS 60/200.R2 balance.

In situ optical microscopy during hygrothermal cycling

Hydration/dehydration cycling was conducted using a humidity generator (Mettler Toledo, MHG-32 MT). The humidity generator featured a deionized water tank and was connected to a dry nitrogen gas supply, enabling the mixing of humid and dry gas for precise humidity control *via* PID. The gas inlet was connected to a custom-built sample chamber which received the regulated (humid/dry) nitrogen. The chamber was equipped

 This journal is © The Royal Society of Chemistry 2025

Open Access Article. Published on 19 August 2025. Downloaded on 2/11/2026 12:09:28 PM.
This article is licensed under a Creative Commons Attribution-NonCommercial 3.0 Unported Licence.

with a transparent quartz window at the top, allowing for *in situ* monitoring of morphological changes of the sample surface during the hygrothermal cycling. Temperature control within the chamber was maintained using a hot plate (Four E'S Scientific, MI0102003). A Keyence VHX Digital Microscope captured images of the specimen every 60 s, using a texture-enhancement mode to clearly highlight morphological changes. The experimental set up of *in situ* imaging can be found in Fig. S2a and b.

The hydration and dehydration conditions suitable for *in situ* imaging were determined based on the phase diagram in Fig. S1, which is derived from the Clausius–Clapeyron relation.[44] As such, we used the hydration conditions of 25 °C and 60% RH, and the dehydration conditions of 80 °C and 0.1% RH, to cycle the system between the dehydrated state and the hydrated state without deliquescence. A 10 min ramping step was applied during humidity and temperature adjustments to prevent abrupt temperature/humidity changes. No evidence of melting, such as liquid phase formation or pellet shape distortion, was observed throughout the measurements. Deliquescence occurred at RH values of $>\sim$70%.

In situ XRD

The crystal structural evolution was investigated with *in situ* X-ray diffraction (XRD, Rigaku Smartlab XE) over a 2θ range of 10° to 50° with a Cu Kα source. Prior to XRD measurements, the $SrCl_2$ samples were prepared as pellets with a diameter of 1 cm and a thickness of $\sim$300 μm. For *in situ* dehydration, an airtight XRD sample chamber (Reactor X) with a dome-shaped cap and an X-ray transparent beryllium window was used to collect XRD data under controlled conditions of 80 °C and 0.1% RH (Fig. S5a). Dry nitrogen was continuously supplied into the chamber to maintain a low-humidity environment. XRD patterns were collected every 6 min, with 5 min required for the XRD scan and 1 min for the detector to return to its starting position.

For *in situ* XRD during hydration, supplying humid air into the chamber directly was not feasible due to water condensation. Instead, fibrous material soaked in water was placed inside the XRD chamber to maintain a humid atmosphere of 40% RH (see Fig. S5b). As with dehydration, XRD patterns were measured every 6 minutes, and the atmospheric conditions were continuously monitored using a temperature and humidity data logger (OMEGA, OM-EL-21CRF-2-LCD). The experimental set up for *in situ* XRD can be found in Fig. S11, and the specific hydration and dehydration conditions are detailed in Fig. S5a and b. It is noted that a 10 min temperature ramping step was incorporated into all hydration and dehydration measurements to ensure gradual adjustments.

Whole pattern fitting was performed based on the following assumptions: (1) all hydrated phases absorb X-rays uniformly and (2) there is no interference or interaction between the different hydrated phases. This analysis was performed using SmartLab Studio II (Rigaku XRD software), with the possible crystal structures pre-selected: $SrCl_2$ (JCPDS: 00-006-0537), $SrCl_2 \cdot H_2O$ (JCPDS: 04-010-2950), $SrCl_2 \cdot 2H_2O$ (JCPDS: 00-025-0891), and $SrCl_2 \cdot 6H_2O$ (JCPDS: 04-010-2982). The software analyzed the pre-selected XRD patterns and generated theoretical (simulated) XRD patterns based on the input crystallographic data. Subsequently, it compared the experimental XRD patterns with the simulated ones, iteratively adjusting parameters to minimize the difference. Finally, it generated the relative weight fraction of each hydrated phase. To ensure accuracy, we took data with a goodness of fit (GoF) and an R_{wp} (weighted profile parameter) value of 15% or below. Additionally, further verification was performed by confirming that the observed changes in the weight percentages of the hydrated phases corresponded to the expected hydration and dehydration reactions. The weight fractions of each hydrated phase were converted to mole fractions to calculate the corresponding volume changes during hydration/dehydration.

The volume change during hydration/dehydration was calculated based on the unit cell volume per Sr for each hydrated phase and normalized by that of the fully hydrated phase. Specifically, the relative volume was determined as follows:

$$\text{Volume change } (\%) = \frac{\text{unit cell volume}}{\text{Sr atoms within the unit cell}} \div \frac{\text{unit cell volume of the hexahydrate}}{1}$$

where 1 represents the number of Sr atom in the hexahydrate phase. It is noted that the unit cells of the anhydrous, monohydrate, and dihydrate phases each contain 4 Sr atoms.

Simultaneous thermal analysis measurements (TGA/DSC)

$SrCl_2$ pellet samples were cut using an X-Acto knife to fit into a 40 μL aluminum crucible with a diameter of $\sim$3 mm. A Mettler Toledo Thermal Analysis System TGA/DSC 3+ was used to monitor the sample mass changes and heat flow during hydration/dehydration cycling. The TGA/DSC system was connected to an MHG 32 Modular Humidity Generator to precisely control temperature and relative humidity conditions of the gas throughout the cycling process. To calibrate the instrument, a reference material with a heat flow comparable to that of $SrCl_2$ ($\sim$1000 J g^{-1}) and within a similar temperature range is needed. Deionized (DI) water was selected as the reference due to its latent heat of vaporization (2260 J g^{-1}). A 40 μL aluminum crucible containing DI water was hermetically sealed with an aluminum lid featuring a 50 μm pinhole and placed in the sample chamber. As the temperature increased, the mass changes and heat fluxes were measured by the instrument, and the system was automatically calibrated using the Mettler STARe software (V17.00). Prior to heat flow and

Open Access Article. Published on 19 August 2025. Downloaded on 2/11/2026 12:09:28 PM.
This article is licensed under a Creative Commons Attribution-NonCommercial 3.0 Unported Licence.

gravimetry measurements, the sample was preconditioned in an environmental chamber at 50 °C and 12% relative humidity for 12 h to ensure the entire sample reached the monohydrate state of $SrCl_2 \cdot H_2O$. For gravimetric and heat flow analysis, temperature was initially kept constant at 25 °C for 10 min to stabilize the sample. Preconditioned nitrogen gas (25 °C and 60% RH) was then flowed into the sample chamber at a rate of 100 mL min^{-1} for 18 h to cause hydration. The temperature was then increased at a rate of 5 °C min^{-1} to 80 °C, and dry nitrogen gas (~0% RH) was flowed to the chamber for ~11.5 h to cause dehydration. The specific temperatures and relative humidity conditions used for these reactions can be found in Fig. S1.

Scanning electron microscope (SEM) imaging

For SEM imaging, the samples were sealed in an N_2-filled glovebox and transferred to the SEM stage (Hitachi SU-8230 SEM) with air exposure <2 min. SEM images were collected using an accelerating voltage of 3 kV.

Author contributions

J. S.: conceptualization, data curation, formal analysis, investigation, methodology, visualization, writing – original draft. M. R. M.: data curation, formal analysis, writing – original draft. E. B.: formal analysis, writing – original draft. A. K. M.: conceptualization, funding acquisition, project administration, resources, supervision, writing – review & editing. M. T. M.: conceptualization, funding acquisition, project administration, resources, supervision, writing – review & editing.

Conflicts of interest

There are no conflicts to declare.

Data availability

Data supporting this article are available upon reasonable request.

The supplementary information file contains additional figures, experimental details, and supporting data, including phase diagrams, experimental setups, images, *in situ* XRD measurements, crystallographic information, and supplementary tables with thermodynamic and kinetic parameters. See DOI: **https://doi.org/10.1039/d5ta02326b**.

Acknowledgements

This material is based upon work supported by the U.S. Department of Energy (DOE), Office of Science under Award # DE-SC0024718. M. R. M. acknowledges the Building Technologies Office (BTO) IBUILD-Graduate Research Fellowship administered by the Oak Ridge Institute for Science and Education (ORISE) (DE-SC0014664) and managed by Oak Ridge National Laboratory (ORNL) (DE-AC05-00OR22725) for the U.S. DOE. This work was performed in part at the Georgia Tech Institute for Matter and Systems, a member of the National Nanotechnology Coordinated Infrastructure (NNCI), which is supported by the National Science Foundation (ECCS-2025462). We thank Prof. Hailong Chen and Guangxing Zhang for helpful discussions.

References

1 N. Nitta, F. Wu, J. T. Lee and G. Yushin, *Mater. Today*, 2015, **18**, 252–264.
2 C. R. Birkl, M. R. Roberts, E. McTurk, P. G. Bruce and D. A. Howey, *J. Power Sources*, 2017, **341**, 373–386.
3 J. Liu, Z. Bao, Y. Cui, E. J. Dufek, J. B. Goodenough, P. Khalifah, Q. Li, B. Y. Liaw, P. Liu and A. Manthiram, *Nat. Energy*, 2019, **4**, 180–186.
4 W. M. Seong, K.-Y. Park, M. H. Lee, S. Moon, K. Oh, H. Park, S. Lee and K. Kang, *Energy Environ. Sci.*, 2018, **11**, 970–978.
5 R. Yazami and Y. F. Reynier, *Electrochim. Acta*, 2002, **47**, 1217–1223.
6 E. A. Olivetti, G. Ceder, G. G. Gaustad and X. Fu, *Joule*, 2017, **1**, 229–243.
7 X. Sun, H. Hao, P. Hartmann, Z. Liu and F. Zhao, *Mater. Today Energy*, 2019, **14**, 100347.
8 Y. Tian, G. Zeng, A. Rutt, T. Shi, H. Kim, J. Wang, J. Koettgen, Y. Sun, B. Ouyang and T. Chen, *Chem. Rev.*, 2020, **121**, 1623–1669.
9 G. Sadeghi, *Energy Storage Mater.*, 2022, **46**, 192–222.
10 J. Xu, R. Wang and Y. Li, *Sol. Energy*, 2014, **103**, 610–638.
11 Z. Ma, X. Wang, P. Davenport, J. Gifford, K. Cook, J. Martinek, J. Schirck, A. Morris, M. Lambert and R. Zhang, *Appl. Therm. Eng.*, 2022, **216**, 119078.
12 A. Odukomaiya, J. Woods, N. James, S. Kaur, K. R. Gluesenkamp, N. Kumar, S. Mumme, R. Jackson and R. Prasher, *Energy Environ. Sci.*, 2021, **14**, 5315–5329.
13 *Nat. Energy*, 2016, **1**, 16193.
14 A. Henry, R. Prasher and A. Majumdar, *Nat. Energy*, 2020, **5**, 635–637.
15 T. Gilbert, A. K. Menon, C. Dames and R. Prasher, *Joule*, 2023, **7**, 128–149.
16 L. Miró, J. Gasia and L. F. Cabeza, *Appl. Energy*, 2016, **179**, 284–301.
17 V. G. Gude, *Appl. Energy*, 2015, **137**, 877–898.
18 G. Alva, Y. Lin and G. Fang, *Energy*, 2018, **144**, 341–378.
19 A. Martin, D. Lilley, R. Prasher and S. Kaur, *Energy Environ. Mater.*, 2024, **7**, e12544.
20 A. Solé, I. Martorell and L. F. Cabeza, *Renew. Sustain. Energy Rev.*, 2015, **47**, 386–398.
21 J. Aarts, H. Fischer, O. Adan and H. Huinink, *J. Energy Storage*, 2024, **76**, 109806.
22 J. Aarts, S. de Jong, M. Cotti, P. Donkers, H. Fischer, O. Adan and H. Huinink, *J. Energy Storage*, 2022, **47**, 103554.
23 H. Lahmidi, S. Mauran and V. Goetz, *Sol. Energy*, 2006, **80**, 883–893.
24 K. E. N'Tsoukpoe, T. Schmidt, H. U. Rammelberg, B. A. Watts and W. K. Ruck, *Appl. Energy*, 2014, **124**, 1–16.
25 A. J. Carrillo, J. González-Aguilar, M. Romero and J. M. Coronado, *Chem. Rev.*, 2019, **119**, 4777–4816.

 This journal is © The Royal Society of Chemistry 2025

Open Access Article. Published on 19 August 2025. Downloaded on 2/11/2026 12:09:28 PM.
This article is licensed under a Creative Commons Attribution-NonCommercial 3.0 Unported Licence.

26 R.-J. Clark, A. Mehrabadi and M. Farid, *J. Energy Storage*, 2020, **27**, 101145.
27 Y. Ding and S. Riffat, *Int. J. Low Carbon Technol.*, 2013, **8**, 106–116.
28 E. Barbosa and A. K. Menon, *J. Energy Storage*, 2024, **90**, 111916.
29 N. Zaleski, E. Barbosa and A. K. Menon, *MRS Energy Sustain.*, 2024, 1–12.
30 S. Kiyabu, P. Girard and D. J. Siegel, *J. Am. Chem. Soc.*, 2022, **144**, 21617–21627.
31 R.-J. Clark, G. Gholamibozanjani, J. Woods, S. Kaur, A. Odukomaiya, S. Al-Hallaj and M. Farid, *J. Energy Storage*, 2022, **51**, 104415.
32 A. U. Rehman, Z. Maosheng and A. Hayat, *Int. J. Energy Res.*, 2020, **44**, 6981–6990.
33 P. A. Kallenberger, K. Posern, K. Linnow, F. J. Brieler, M. Steiger and M. Fröba, *Adv. Sustain. Syst.*, 2018, **2**, 1700160.
34 B. Tian, Z. Jin, L. Wang and R. Wang, *Int. J. Heat Mass Tran.*, 2012, **55**, 4453–4459.
35 P. A. Kallenberger, F. J. Brieler, K. Posern and M. Fröba, *Chem. Ing. Tech.*, 2016, **88**, 379–384.
36 H. Huang, J. Li, Y. O. Huhetaoli, C. Wang, N. Kobayashi, Z. He and L. Deng, *Energy Technol.*, 2016, **4**, 1401–1408.
37 M. A. Blijlevens, N. Mazur, W. Kooijman, H. R. Fischer, H. P. Huinink, H. Meekes and E. Vlieg, *Sol. Energy Mater. Sol. Cells*, 2022, **242**, 111770.
38 R. Fisher, Y. Ding and A. Sciacovelli, *J. Energy Storage*, 2021, **38**, 102561.
39 M. Gaeini, S. Shaik and C. Rindt, *Energy Build.*, 2019, **196**, 178–193.
40 L.-C. Sögütoglu, M. Steiger, J. Houben, D. Biemans, H. R. Fischer, P. Donkers, H. Huinink and O. C. Adan, *Cryst. Growth Des.*, 2019, **19**, 2279–2288.
41 A. Shkatulov, J. Houben, H. Fischer and H. Huinink, *Renew. Energy*, 2020, **150**, 990–1000.
42 W. Li, H. Guo, M. Zeng and Q. Wang, *Energy Convers. Manage.*, 2019, **198**, 111843.
43 N. Mazur, I. Kotinis, H. Huinink, H. Fischer and O. Adan, *Sol. Energy Mater. Sol. Cells*, 2024, **268**, 112748.
44 L. Glasser, *J. Chem. Eng. Data*, 2014, **59**, 526–530.